Resistance Mechanisms of Articulated Tracked All-Terrain Vehicles in Complex Hydrodynamic Conditions

Zhanlong Li, Zizhou Wang, Zheng Zhang, Hairui Sun, and Pengxiang Hao

***Abstract*—Articulated tracked all-terrain vehicles offer excellent off-road mobility and high load-carrying capacity, allowing them to adapt to diverse operating environments. However, the complexity of their tracked propulsion systems makes it difficult to predict water resistance during aquatic operations. The vehicle's hydrodynamic performance in water has a direct impact on the success of rescue missions and, of greater significance, on the safety of both rescuers and those being rescued. In this study, based on a specific type of articulated tracked all-terrain vehicle, a hydrodynamic model was established using the Realizable k-ε turbulence model and multi-body overlapping mixed grid division to investigate water resistance effects under different vehicle models, as well as the dynamic water resistance characteristics under varying speeds and loads. The results indicate that the track structure constitutes the primary source of underwater resistance in the vehicle's propulsion system, and an enclosed track design can reduce water resistance by approximately 49%. Both the vehicle's navigation speed and load mass show a positive correlation with water resistance, with variations in speed exerting a more pronounced impact on resistance. These findings propose effective strategies for optimizing the design of articulated all-terrain vehicles and offer theoretical guidance for ensuring safety during water navigation.**

Index Terms*—*Articulated; All-Terrain Vehicle; Still-Water Na vigation; Resistance Characteristics

I. INTRODUCTION

The frequent occurrence of extreme weather events and public safety incidents worldwide in recent years has revealed the limitations of existing emergency rescue equipment in complex disaster scenarios. This highlights the pressing need to establish a highly mobile, multi-functional emergency rescue system capable of responding to all types of disasters[1]. Harsh road conditions caused by extreme weather—such as mudslides, flash floods, and landslides—frequently hinder rescue vehicles from accessing disaster sites, thereby significantly reducing rescue efficiency. The development of a high-speed, heavy-duty platform for emergency rescue vehicles with multi-terrain adaptability is of critical importance. To ensure high mobility across complex terrains, ATVs commonly employ tracked propulsion systems. However, the drag associated with these complex tracked systems and vehicle structures during underwater navigation restricts the maneuverability of ATVs in aquatic environments, thereby posing significant challenges for water-based rescue operations. Therefore, investigating the application of amphibious ATVs in large-scale and multi-condition underwater rescue operations is crucial [2]. Among these, water resistance characteristics constitute a key performance indicator for amphibious ATVs during underwater navigation [3]. Research on these characteristics is vital to ensure that such vehicles demonstrate optimal hydrodynamic performance in varying underwater rescue environments [4].

The main methods for analyzing the resistance characteristics of amphibious all-terrain vehicles are full-scale vehicle experiments and computer simulations [5-6]. Compared to full-scale vehicle testing, computer simulation offers greater convenience, faster results, and lower costs [7-9]. Both domestic and international researchers have conducted a series of studies on this topic. Maimun [10], aimed at enhancing the hydrodynamic performance of amphibious vehicles, investigated three new bow designs and employed CFD simulations to investigate hydrodynamic phenomena across a range of speeds. Zhangxia Guo [11] emphasized the significance of vehicle speed for amphibious vehicles, while highlighting the limitations of traditional towing tank resistance tests, and suggested that CFD simulation serves as an ideal method for predicting and optimizing vehicle speed during the design phase. Tao Wang [12] from the Academy of Armored Forces Engineering conducted simulations of viscous flow fields around amphibious vehicles without considering the free surface. They obtained clear visual results and detailed flow field data, finding that the pressure distribution in the simulated and experimental flow fields was largely consistent, demonstrating the feasibility of the simulations. Li [13] from the Academy of Armored Forces Engineering employed unstructured grids, a two-equation k-ε turbulence model, and the finite volume method to solve the velocity and pressure fields of an amphibious vehicle model, to predict navigation resistance and conduct flow field visualization analysis. Xin [14] took into account the effects of wheel rotation and utilized simulations to predict and improve the vehicle's performance under real-world water-wading conditions,

Manuscript received November 9, 2024; revised February 18, 2025.

This study was supported by The Xinzhou City Science and Technology Plan Project - Key Research and Development Plan (Grant No. 20220107), the National Natural Science Foundation of China (Grant Nos. 52205212 and 52272401), the Fundamental Research Program of Shanxi Province (Grant No. 202203021211185), the Shanxi Students' Platform for Innovation and Entrepreneurship Training Program (Grant No. 20230671), and the Guizhou Province Science and Technology Plan Project - Science and Technology Innovation Talent Team (CXTD [2022]015).

Zhanlong Li is an associate professor at the School of Vehicle and Transportation Engineering, Taiyuan University of Science and Technology, Taiyuan 030024, China. (e-mail: lizl@tyust.edu.cn).

Zizhou Wang is a postgraduate from the School of Vehicle and Transportation Engineering, Taiyuan University of Science and Technology, Taiyuan 030024, China (e-mail: 437490694@qq.com).

Zheng Zhang is a postgraduate from the School of Vehicle and Transportation Engineering, Taiyuan University of Science and Technology, Taiyuan 030024, China (e-mail: 598717937@qq.com).

Hairui Sun is a postgraduate from the School of Vehicle and Transportation Engineering, Taiyuan University of Science and Technology, Taiyuan 030024, China (e-mail: 284910524@qq.com).

Pengxiang Hao is an engineer at the Guizhou Zhanyang Kinetics Co., Ltd., Guizhou, Guiyang 550006, China (e-mail: haopengxiang@jonyanng.com).

offering theoretical guidance for the early design stages of wading performance improvement. Amini [15] investigated the influence of vehicle speed on hydrodynamic coefficients and recommended the use of estimation functions instead of fixed coefficients to accurately predict vehicle behavior. Existing research has provided a foundation for the simulation of water resistance characteristics in all-terrain vehicles.

The articulated tracked all-terrain vehicle, as a twin-body structure, is composed of two non-streamlined tracked compartments which are connected by an articulated joint. The hydrodynamic forces generated by the front and rear vehicle bodies during water movement mutually interfere and impact the vehicle's overall navigation performance. This study focuses on a specific articulated tracked all-terrain vehicle (as shown in Figure 1), examining the hydrodynamic effects of different model structures and investigating the characteristics of water resistance under various operating conditions, aiming to identify key factors influencing resistance and propose solutions for drag reduction optimization. Based on this, the study evaluates the impact of waves generated by the vehicle's front during operation on the driver's visibility and provides specific driving recommendations to improve vehicle safety and practical performance. This research offers valuable insights into the design improvements of articulated tracked all-terrain vehicles (hereafter referred to as all-terrain vehicles) and contributes to their broader application in demanding operational environments.

Fig. 1. Vehicle model.

II. Hydrodynamic Modeling of All-Terrain Vehicles

The water resistance of all-terrain vehicles is predominantly determined by three factors: the tracked mechanism, vehicle body shape, and accessories. As a core component of the all-terrain vehicle, the structural refinement of the tracked mechanism plays a particularly crucial role in water resistance. Based on varying levels of refinement, three models were established as shown in Fig 2. Model 1 (Fig 2a) treats the propulsion system as a completely enclosed structure. In Model 2 (Fig 2b), the support wheel structure is refined, while the track structure is retained as a whole. Model 3 (Fig 2c) further refines the track link structure of the propulsion system. In Fig 2, Region A represents the front part of each vehicle model and the water area in front of it, including the water flow area along the front sides of the vehicle. Region B covers the articulated position at the middle of each vehicle and the surrounding water area. Region C includes the rear part of each vehicle and the water at its sides and behind the vehicle. he total length of the all-terrain vehicle model is L_m = 17.8 meters.

Overlapping grid technology is used to analyze the effect of the vehicle body shape on water flow and to capture dynamic changes in the flow field. Based on the global grid, a four-layer expanded grid refinement is implemented at the contact surface between the vehicle and its external environment. To enhance simulation accuracy and reduce computation time, denser tetrahedral grids are applied in the areas near the vehicle body, while sparser tetrahedral grids are used in the outer flow field regions farther from the vehicle. The fluid domain extends 2.5L_m in the longitudinal direction and 1.5L_m in the lateral direction. The boundary conditions consist of one velocity inlet and two pressure outlets. The velocity inlet is set to oppose the direction of the vehicle's movement, while the pressure outlets are located downstream of the vehicle's motion and at the top of the vehicle. A gravitational acceleration of 9.81 m/s² is applied in the vertical direction, with standard atmospheric pressure serving as the reference pressure.

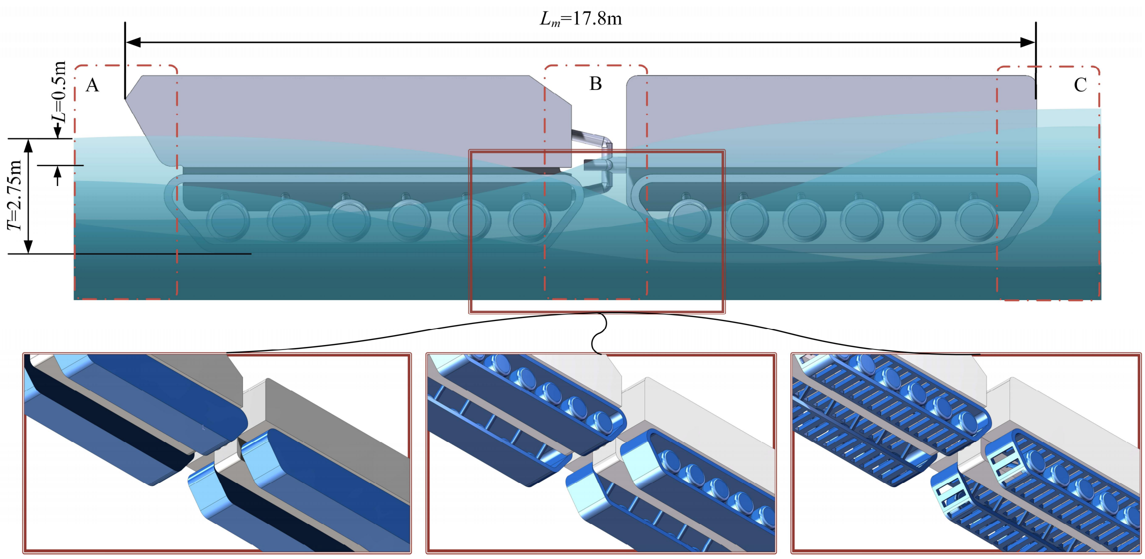

(a) Model 1 (b) Model 2 (c) Model 3

Fig. 2. Simplified models of the all-terrain vehicle

III. Hydrodynamic Effects of All-Terrain Vehicle

Hydrodynamic effects refer to the series of fluid dynamic phenomena that occur when water interacts with an object. In different refined models, changes in the vehicle's structure cause disturbances in the free surface, variations in flow separation patterns, and differences in pressure distribution. These factors collectively influence the vehicle's overall resistance performance.

A. Free Surface Fluctuation Characteristics

The fluctuation characteristics of the free liquid surface reflect the dynamic behavior of the interaction between the vehicle and the water body, which is a critical factor influencing drag changes. When the vehicle moves at a speed of 3 m/s, the resulting free surface water ripples are shown in Fig 3.

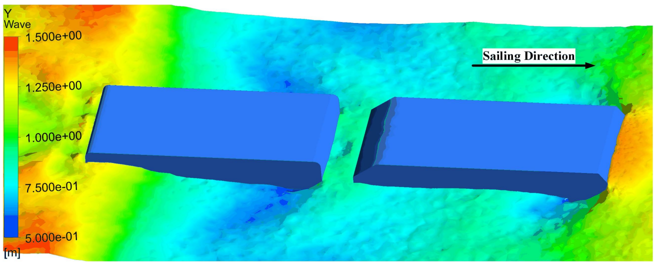

(a) Model 1

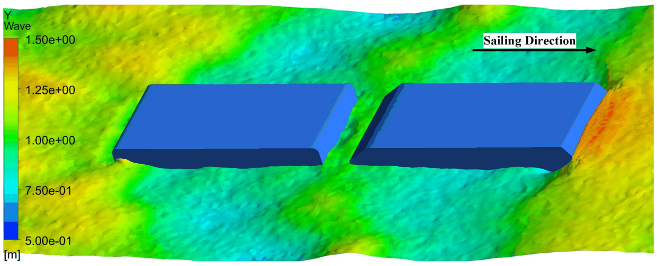

(b) Model 2

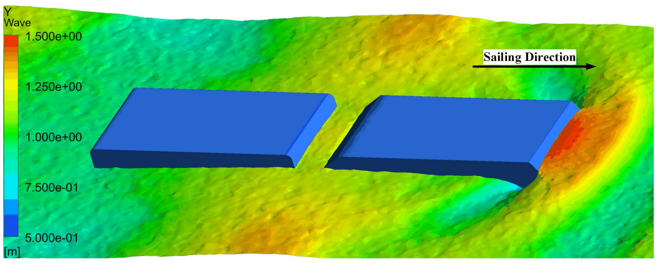

(c) Model 3

Fig. 3. Vehicle model.

The front of the carriages in all three models produced wave crests that spread to both sides, forming water waves; however, there were differences in wave characteristics. In Model 1, the waves had a radial conical shape, with superimposed waves at the rear of the vehicle forming a wave crest. In Model 2, scattered waves on the vehicle's sides increased and superimposed, resulting in a reverse radial conical distribution, opposite to the direction of the vehicle's movement. Model 3 exhibited both wave peaks and troughs in Region A, with wave height in Region B above average. Specific data for wave peaks and troughs are presented in Table 1.

TABLE I
Wave Crest and Trough Values

Model	Parameter	Value/m
	Distance from Wave Crest to Free Surface	0.33
Model 1	Distance from Wave Trough to Free Surface	0.21
	Distance from Wave Crest to Vehicle Roof	0.12
	Distance from Wave Crest to Free Surface	0.37
Model 2	Distance from Wave Trough to Free Surface	0.38
	Distance from Wave Crest to Vehicle Roof	0.08
	Distance from Wave Crest to Free Surface	0.40
Model 3	Distance from Wave Trough to Free Surface	0.40
	Distance from Wave Crest to Vehicle Roof	0

The crests are caused by the compression of water flow at the front of the vehicle as it splits the water and moves forward, leading to the accumulation of water. Wave troughs, on the other hand, are primarily caused by the oversized edges on both sides of the vehicle and the effect of surface tension. The traveling mechanism of Model 1 features a completely enclosed monolithic structure, and its enclosure reduces water leakage and interference at the bottom and sides of the vehicle. The refined supporting wheel structure in Model 2 increases the complexity of the fluid channel and intensifies water flow disturbances, causing the superposition and diffusion of water waves on both sides of the vehicle. Compared to Model 1, Model 2 has wave crests that are 12% higher and wave troughs that are 80% lower. The refinement of the track link structure in Model 3 increases the local passage path between the vehicle's traveling mechanism and the water flow. However, because the effect of the link structure on water flow is confined to a small gap region, the change in disturbance intensity on the free liquid surface is small compared to the large-scale disturbance caused by the supporting wheel structure in Model 2. The wave crest in Model 3 is 8% higher and the trough is 5% lower than in Model 2.

The refinement level of the vehicle model is positively correlated with the disturbance intensity of the free surface. Although the disturbance caused by Model 3 is weaker, the wave crest height in Model 3 aligns with the vehicle's roof, causing the driver's observation window to be flooded during operation. This severely impairs the driver's visibility and presents a significant safety risk. Changes in free surface disturbance are an external manifestation of the interaction between the vehicle and the water body, fundamentally driven by variations in the flow separation around the vehicle. Different refined model structures not only alter the wave patterns on the free surface but also influence the flow patterns around the vehicle body. To further analyze the hydrodynamic effects, the following section will examine flow separation around the vehicle.

B. Water Flow Patterns Around the Vehicle Body

During the navigation of the all-terrain vehicle, flow separation and vortex formation as the water flows around the vehicle are the primary reasons for the significant increase in navigation resistance. The flow characteristics are shown in Figures 4-6. The flow patterns in the horizontal plane of the vehicle body visualize the overall flow characteristics and their influence on the increase in resistance, while the flow field diagram in the vertical plane further reveals the root cause of flow formation and its specific impact on differential pressure drag.

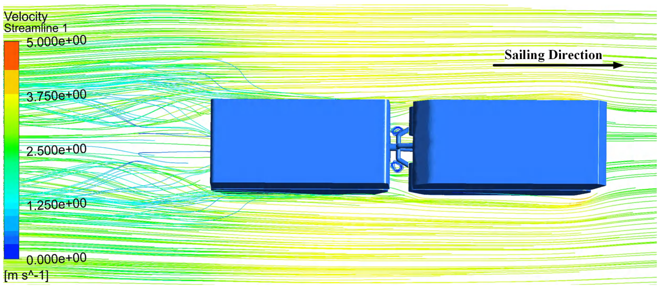

(a) Horizontal flow separation diagram of the vehicle body

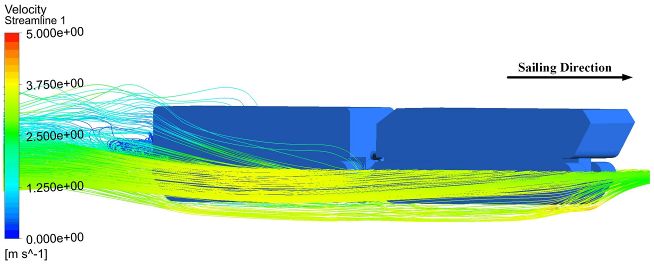

(b) Vertical flow field diagram of the tracked mechanism
Fig 4. Flow separation characteristics of Model 1

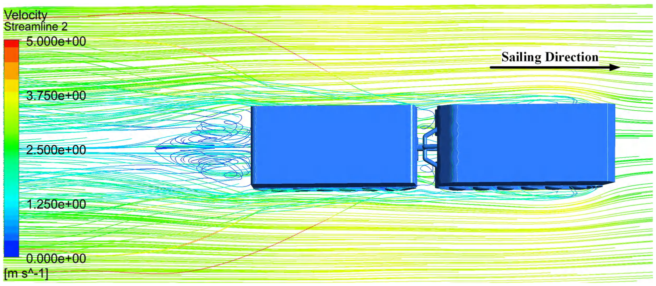

(a) Horizontal flow separation diagram of the vehicle body

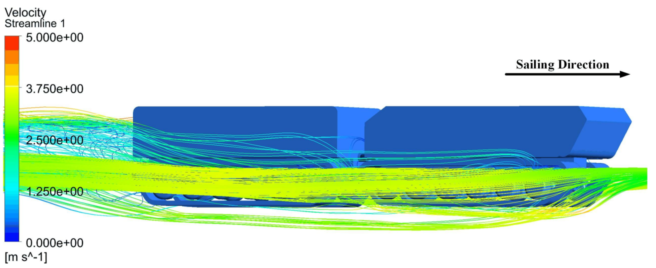

(b) Vertical flow field diagram of the tracked mechanism
Fig 5. Flow separation characteristics of Model 2

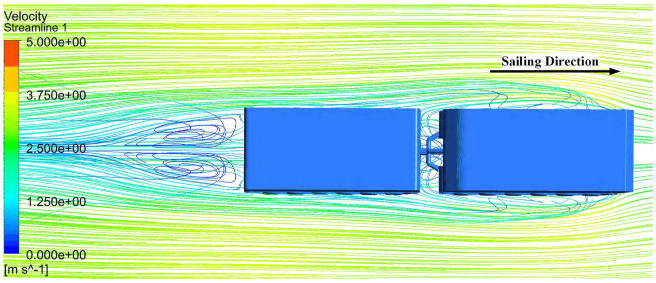

(a) Horizontal flow separation diagram of the vehicle body

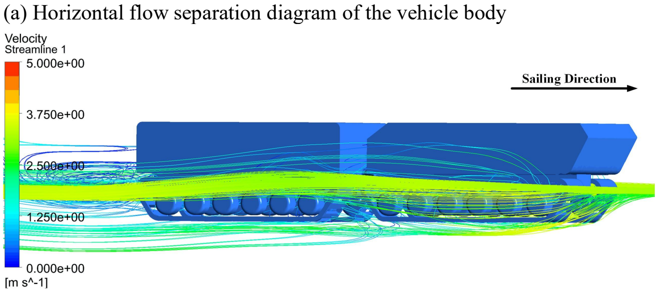

(b) Vertical flow field diagram of the tracked mechanism
Fig 6. Flow separation characteristics of Model 3

As shown in Figure 4, in Model 1, the water flow bypasses both sides of the tracked traveling mechanism and passes directly through the chassis, with significant vortex formation occurring at the articulation point. The flat design of the traveling mechanism does not form an effective obstruction to the water flow, resulting in high kinetic energy but low disturbance to the water flow. The water velocity reaches approximately 2.9 m/s in the sump region. However, due to the complex structure of the articulation, the fast water flow undergoes fluid separation in this region, forming a significant vortex structure.

As shown in Figure 5, in Model 2, the water flows around both sides of the track and through the chassis, then returns to the supporting wheel region. Multiple load wheels, axles, and other structures inside the track create additional obstructions to the water flow, increasing vortex losses and reducing the flow velocity around both sides of the vehicle to 1.4 m/s. A closed vortex structure is formed in the rear part of the vehicle, which slows the flow velocity to 0.3 m/s, leading to a significant energy loss in the tail flow region.

The flow in Model 3 is more complex, as shown in Figure 6. The water not only flows around both sides of the track but also enters the support wheel area through the track link through-hole. This diversifies the flow path, further expanding the range of the flow velocity slowdown. A large turbulent area forms on the side of the vehicle, and the irregular elliptical vortex in the rear of the vehicle increases. A comparison of the winding characteristics of the three models reveals that the complex track structure increases fluid channel complexity and causes vortex losses, which is unfavorable to the vehicle's hydrodynamic performance. To improve the vehicle’s in-water performance, it is recommended to optimize the track structure design to reduce internal obstructions and vortex formation.

Changes in the water flow path induce flow separation and the formation of vortices and eddies, altering the flow separation patterns and subsequently affecting the pressure distribution around the vehicle. The following section analyzes the pressure distribution on the vehicle’s surface and its specific impact on navigation resistance.

C. Pressure Resistance Characteristics

The pressure distribution on the surface of the vehicle directly influences the water flow force, which is closely related to changes in navigation resistance. There are differences in the degree of refinement of the traveling mechanism in each model, and the pressure analysis is conducted by considering the free liquid surface near the vehicle chassis at a depth of L = 0.5 m. The pressure cloud diagrams for the three models are shown in Figure 7.

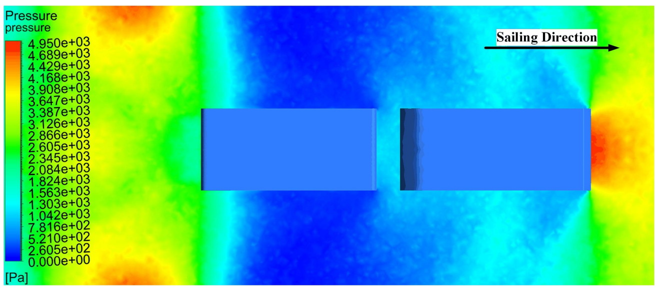

(a) Model 1

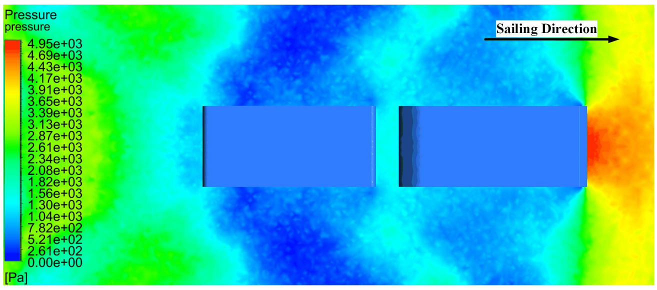

(b) Model 2

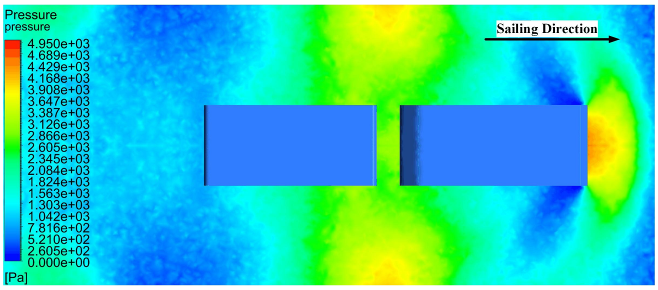

(c) Model 3

Fig 7. Pressure contour lot at a free surface depth of 0.5 m

As shown in Figure 7, the pressure distributions for the three models traveling in water exhibit significant regional differences. Region A consistently shows a high-pressure zone, with pressure values ranging from 4915 Pa to 5653 Pa. The front of the vehicle experiences significant frontal drag due to the incoming flow. Compared to Model 1, Model 2 shows a slight increase in pressure in Region A to 5653 Pa. This increase is primarily due to the refined part of the support wheel structure obstructing the water flow path, which results in higher pressure at the vehicle's front. In Model 3, the open track through-hole design provides an additional drainage path for the water flow, reducing the pressure concentration at the front, thereby lowering the pressure in Region A to 4915 Pa. The pressure in Region B is affected by the superposition of the low pressure from the front tail flow and the high pressure from the rear incoming flow. As the refinement of the traveling mechanism increases, the pressure in Region B gradually increases. In contrast, the pressure in Region C decreases with increasing model complexity, and the pressure in Region C for Model 3 is only 926 Pa. The pressure data for each region are shown in Table 2.

TABLE II
PRESSURE DATA AT FREE SURFACE DEPTH OF 0.5 M

Model	Parameter	Value/Pa
Model 1	Pressure in Region A	5393
	Pressure in Region B	1026
	Pressure in Region C	2489
Model 2	Pressure in Region A	5653
	Pressure in Region B	1318
	Pressure in Region C	1083
Model 3	Pressure in Region A	4915
	Pressure in Region B	2941
	Pressure in Region C	926

The pressure distribution varies across the three models, and these variations result in pressure differences between regions, which are the primary source of navigation resistance. The pressure differences between regions for the different models are shown in Table 3.

TABLE III
PRESSURE DIFFERENCE DATA AT FREE SURFACE DEPTH OF 0.5 M

Model	Parameter	Value/Pa
Model 1	Pressure Difference Between Regions A-B	4367
	Pressure Difference Between Regions B-C	-1463
Model 2	Pressure Difference Between Regions A-B	4335
	Pressure Difference Between Regions B-C	235
Model 3	Pressure Difference Between Regions A-B	1974
	Pressure Difference Between Regions B-C	2015

The differences in pressure distribution among the three models significantly impact the navigation resistance. In Model 1, the pressure difference in the front vehicle (Region A-B) is 4367 Pa, and the pressure difference in the rear vehicle (Region B-C) is -1463 Pa. This negative pressure difference effectively counteracts part of the navigation resistance, keeping the total navigation resistance at a low 17,800 N. In contrast, in Model 2, the pressure difference in the front vehicle slightly decreases to 4335 Pa, while the negative pressure difference in the rear vehicle becomes a positive pressure difference of 235 Pa, increasing the total navigation resistance. In Model 3, the differential pressure of the front vehicle further decreases to 1974 Pa, while the differential pressure of the rear vehicle increases to 2015 Pa, significantly increasing the aft resistance and raising the total resistance to 35,100 N. Overall, with the refinement of the tracked mechanism, the pressure difference at the front of the vehicle gradually decreases, partially alleviating the frontal resistance. However, the continuous increase in positive pressure difference at the rear elevates the rear resistance, ultimately resulting in a significant rise in total navigation resistance.

TABLE IV
NAVIGATION RESISTANCE CHARACTERISTICS OF DIFFERENT MODELS

Model	Resistance/N	Total Resistance Coefficient	Difference from the Previous Model
Model 1	17800	0.012	-
Model 2	33500	0.019	88.20%
Model 3	35100	0.020	4.78%

The sailing resistance data are shown in Table 4. The difference in sailing resistance between Model 1 and Model 2 is significant, with a difference of 88.2%, with Model 2 exhibiting greater resistance. In contrast, the difference in sailing resistance between Model 2 and Model 3 is smaller, with Model 3's resistance only 4.78% higher than that of Model 2. The results indicate that refining the shape of the traveling mechanism can significantly reduce the vehicle's sailing resistance, while the track link structure refinement has less effect on resistance. To enhance the vehicle's aquatic performance, it is recommended to optimize the track structure design to minimize internal obstructions and vortex formation. Vehicle resistance can be reduced by sealing the traveling mechanism or adding smooth outer panels.

IV. INVESTIGATION OF WATER RESISTANCE CHARACTERISTICS UNDER VARYING CONDITIONS

Based on all-terrain vehicle Model 3, the water resistance characteristics of all-terrain vehicles are investigated under varying working conditions, including different load masses (36 tons, 44 tons, 52 tons, and 60 tons) and sailing speeds (0.5 m/s, 1 m/s, 1.5 m/s, 2 m/s, 2.5 m/s, and 3 m/s) on water.

A. Hydrodynamic Behavior of Water Flow Around the Vehicle

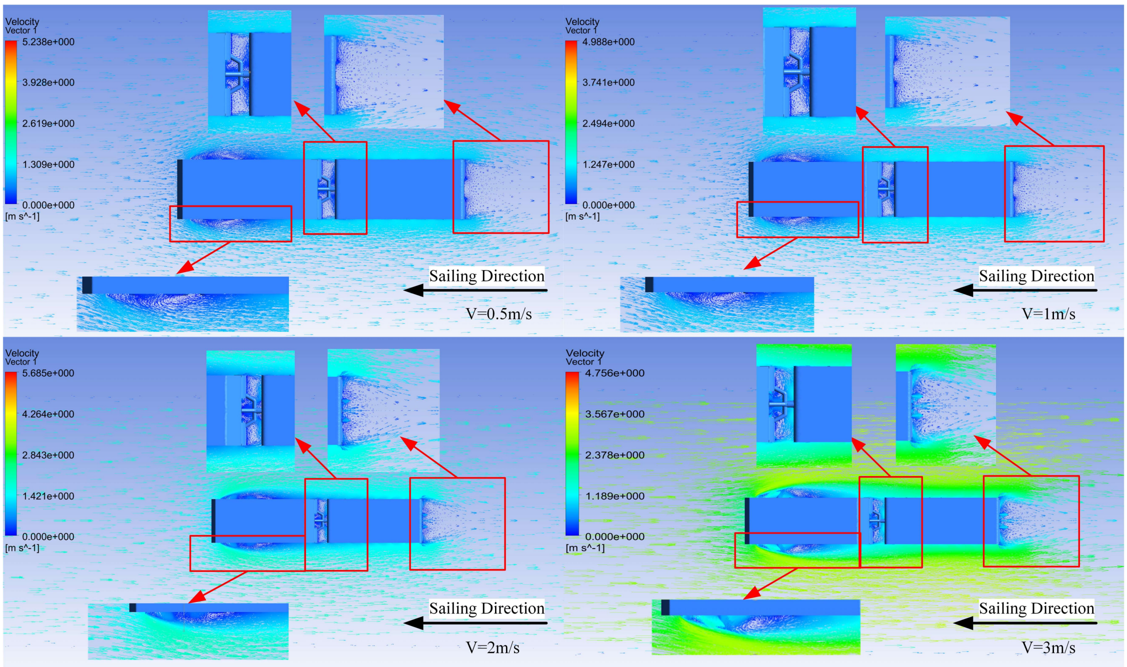

Fig 8. Flow separation velocity vector diagram of the all-terrain vehicle under varying speeds

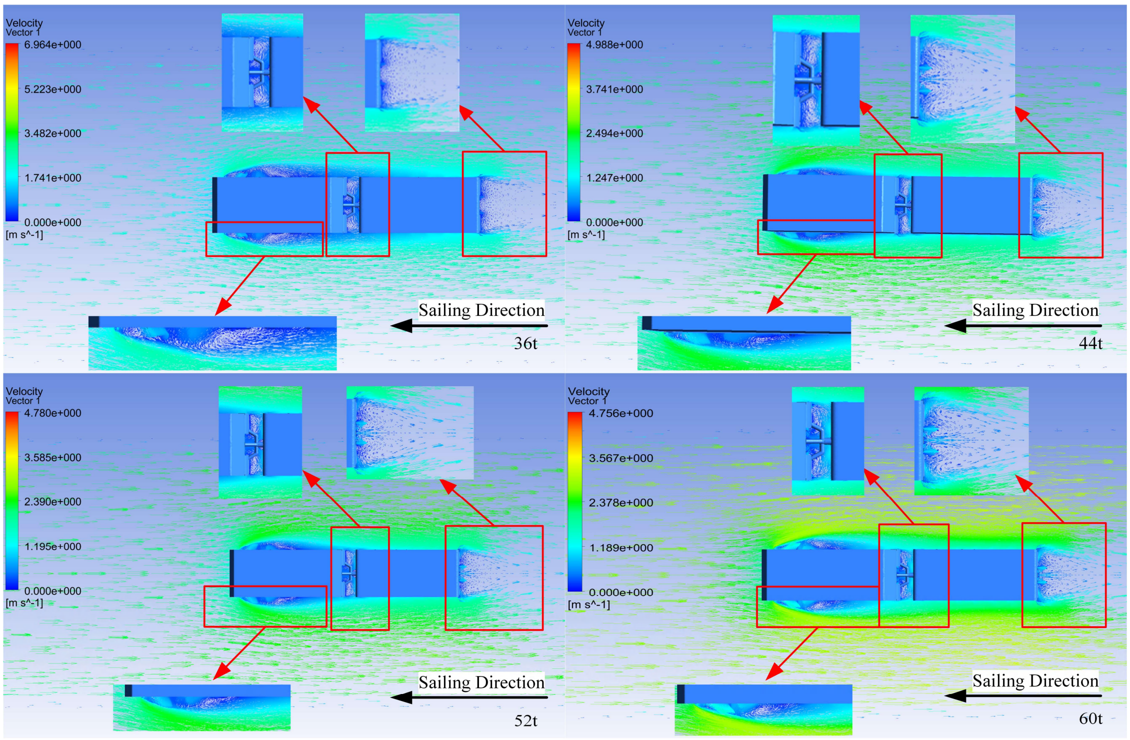

Fig 9. Flow separation velocity vector diagram of the all-terrain vehicle under different load masses

The streamflow around the all-terrain vehicle at different speeds, including the front, middle, and rear regions (Regions A, B, and C), is illustrated in Figure 8. As the streamflow passes the vehicle, boundary layer effects cause flow detachment in Region A, partial reattachment in Region B, and wake contraction in Region C. Under low-speed conditions (0.5 m/s), the flow is dominated by regular laminar flow, with strong fluid attachment, a large wake region, minimal local vortex formation, and improved flow stability. As speed increases, particularly at 3 m/s, the streamflow transitions from laminar to turbulent, with frequent detachment and reattachment. This results in intensified vortex strength in Region B, more pronounced wake contraction in Region C, increased turbulence, reduced hydrodynamic performance, and greater vortex-induced energy losses.

The flow separation phenomena under different load masses are shown in Figure 9. Under light load conditions (36 tonnes), boundary layer separation in Region A is minimal, fluid disturbances in Regions B and C are weak, the wake region is compact, and the flow separation velocity is low. As the load mass increases to 60 tons, the flow separation velocity in Region B increases significantly, and the negative pressure effect intensifies, causing the fluid to accelerate and reattach at the rear articulated joint of the vehicle. Wake separation worsens, and vortex intensity and turbulence in Region C increase substantially.

During aquatic navigation, the dense streamlines around the front of the vehicle lead to the formation of wave crests. The height of these wave crests not only affects resistance characteristics but can also obstruct the driver’s field of vision. When the wave crest becomes too high, the driver’s view is blocked by the water, making it difficult to judge direction and landing position, which increases navigation risks. The maximum wave height data at the front of the vehicle under different operating conditions are presented in Table 4.

TABLE V
WAVE HEIGHTS AT DIFFERENT LOAD MASSES AND SPEEDS

Speed (m/s)	Load Mass (tons)			
	36	44	52	60
0.5	0.78 m	0.85 m	0.93 m	1.04 m
1.0	0.85 m	1.05 m	1.12 m	1.22 m
1.5	1.06 m	1.12 m	1.21 m	1.32 m
2.0	1.12 m	1.17 m	1.30 m	1.41 m
2.5	1.17 m	1.23 m	1.43 m	1.49 m
3.0	1.24 m	1.32 m	1.51 m	1.59 m

As seen in Table 5, the wave height increases gradually with vehicle speed. When the vehicle mass is 60 tonnes and the speed is 1.5 m/s, the wave crest reaches 1.32 m, providing the driver with good visibility during aquatic navigation. However, when the speed increases to 2 m/s, the wave crest rises to 1.41 m, blocking about 25% of the driver’s view, leading to increased frontal drag.

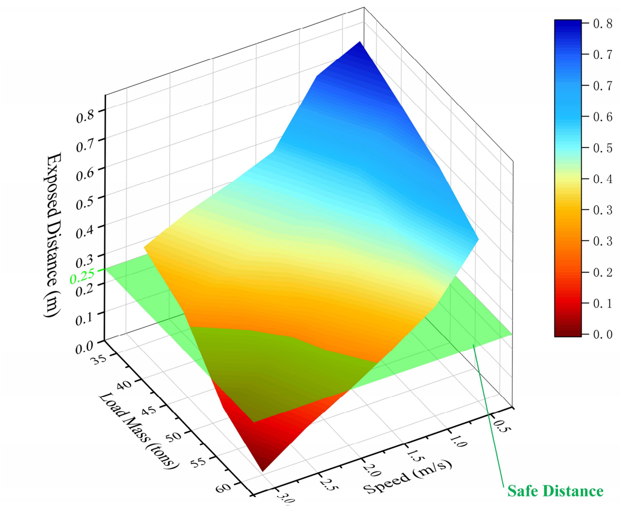

Fig 10. Variation of exposed distance with varying load masses and speeds

Based on ergonomic principles and the vehicle's structural design, the exposed distance (the vertical distance between the driver's window and the water surface) should be no less than 0.25 m. The safe driving conditions are shown in Figure 10. As seen in Figure 10, when the sailing speed is 3 m/s, a vehicle mass greater than 44 tons results in excessive wave crests, which negatively impact both the driver’s visibility and vehicle resistance. When the vehicle mass reaches 60 tons, the sailing speed should not exceed 2 m/s to prevent the adverse effects of increased wave crests, which would restrict visibility, raise navigational risks, and further increase resistance.

B. Characteristics of Navigation Resistance

The sailing resistance characteristics for different load masses and speeds are shown in Table 5. As illustrated in Table 6, resistance tends to increase with both mass and speed. Under low-speed conditions (v = 0.5 m/s), resistance increases by approximately 21.4% when the load mass increases from 44 tons to 52 tons, indicating that resistance is particularly sensitive to changes in load mass. However, an inflection point occurs in the rate of resistance increase when the speed reaches 1.5 m/s, at which point the effect of load mass on resistance diminishes as speed increases. In contrast, the effect of speed on resistance becomes more significant, particularly at 2.5 m/s and 3.0 m/s, where resistance increases rapidly due to enhanced current disturbances. At a speed of 3.0 m/s, resistance increases by as much as 52%, indicating that high-speed turbulence significantly impacts hydrodynamic performance.

TABLE VI
RESISTANCE CHARACTERISTICS UNDER VARYING LOAD MASSES AND SPEEDS

Speed (m/s)	Load Mass (tons)			
	36	44	52	60
0.5	1320 N	1540 N	1870 N	2120 N
1.0	3980 N	4320 N	4710 N	5240 N
1.5	8020 N	8840 N	9250 N	9600 N
2.0	11200 N	12400 N	13800 N	14900 N
2.5	18300 N	19500 N	21300 N	23140 N
3.0	26600 N	28400 N	32500 N	35100 N

V. CONCLUSIONS

This paper investigates the water resistance effect of different models of articulated tracked all-terrain vehicles. The bypass flow, wave height, and resistance characteristics are analyzed under varying conditions of load mass and travel speed, leading to the following conclusions:

(1) The refinement of the support wheel in the traveling mechanism increases the complexity of the fluid channel, significantly enhancing the disturbance of the free liquid surface. This results in a 12% increase in wave peak height and an 80% reduction in wave trough, intensifying the superposition and diffusion of water waves on both sides of the vehicle. The closed vortex structure at the rear of the vehicle reduces the winding velocity to 1.4 m/s and increases vortex energy loss. The front head-on pressure rises to 5653 Pa, intensifying frontal resistance. Additionally, the negative pressure difference at the rear becomes a positive value of 235 Pa, significantly increasing aft drag and resulting in an 88.20% increase in sailing resistance.

(2) The effect of track link refinement on drag is relatively minor, with total drag increasing by only 4.78%. The disturbance of the free fluid surface is weakened, with the crest height rising by only 8% and the trough decreasing by 5%. However, the irregular vortex at the rear of the vehicle enlarges, enhancing turbulence intensity and increasing energy loss. The front pressure decreases to 4915 Pa, alleviating frontal drag, but the positive pressure difference at the rear increases to 2015 Pa, making the rear drag the primary source of increased resistance.

(3) Increases in mass and speed significantly affect the resistance characteristics of all-terrain vehicles. Speed increase shifts the flow around the vehicle from laminar to turbulent, and the increase in load mass further amplifies the intensity of vortices and wake. Under low-speed conditions (0.5 m/s), resistance is more sensitive to changes in load mass. Under high-speed conditions (3.0 m/s), speed becomes the dominant factor, leading to a 52% increase in resistance. Proper adjustment of load mass and speed can effectively optimize hydrodynamic performance and reduce resistance.

(4) To ensure the vehicle's navigation safety, the load mass

should not exceed 44 tonnes at a sailing speed of 3 m/s. When the load mass reaches 60 tonnes, the speed should be controlled within 2 m/s to maintain the clarity of the driver's field of vision and the stability of the vehicle's maneuvering.

In conclusion, although articulated tracked all-terrain vehicles have excellent carrying capacity, the complex traveling mechanism increases navigational resistance, which limits speed and reduces fuel efficiency. The combined effect of load mass and speed on resistance should be comprehensively considered to optimize the vehicle's hydrodynamic performance. Future research should focus on optimizing the shape of the traveling mechanism and exploring the feasibility of resistance-reducing designs (e.g., drag-reducing fins or deflector shields) to further enhance the vehicle's efficiency and safety in water.

REFERENCES

[1] Rane P, Premkumar T M, Hariram V. "Stability investigation of SLV in amphibious mode using forces calculated by employing CFD model," Materials Today: Proceedings, vol. 33, pp4550-4556, 2020

[2] Shirsath P S, Hajare M S, Sonawane G D, Kuwar A, Gunjal S. "A review on design and analysis of amphibious vehicle," International Journal of Service Technology and Management, vol. 4, no. 1, pp43-58, 2015

[3] Jang J Y, Liu T L, Pan K C. "Numerical investigation on the hydrodynamic performance of amphibious wheeled armored vehicles," Journal of the Chinese Institute of Engineers, vol. 42, no. 8, pp700-711, 2019

[4] Annati M. "Amphibious vehicles: The ship to shore objective," Military Technology, vol. 39, no. 9, pp114-118, 2015

[5] Faltinsen O M. Hydrodynamics of High-Speed Marine Vehicles, Cambridge: Cambridge University Press, 2005

[6] More R R, Adhav P, Senthilkumar K, Trikande M W. "Stability and drag analysis of wheeled amphibious vehicle using CFD and model testing techniques," Applied Mechanics and Materials, vol. 592-594, pp1210-1219, 2014.

[7] Wang Y, Chen H Y, Wang T L, et al. "Numerical and experimental analysis of the navigation attitude of vector waterjet propelled amphibious vehicles," Acta Armamentarii, vol. 43, no. 6, pp1120-1128, 2022.

[8] Li L, Wang X, Han S, Wang P. "Calculation of wave-making resistance and analysis of flow field for amphibious armored vehicles," Acta Armamentarii, vol. 31, no. 8, pp1102-1105, 2010

[9] Wang T, Xu G, Yao X, Zhou J. "Numerical simulation of two-phase flow field around amphibious vehicle and analysis of power performance on water," Journal of Mechanical Engineering, vol. 44, no. 12, pp168-172, 2008

[10] Maimun A, Nakisa M, Tarmizi A. "Numerical study on hydrodynamic resistance of new hull design for multipurpose amphibious vehicle," Applied Mechanics and Materials, vol. 663, pp522-531, 2014

[11] Guo Zhangxia, Li Kuiwu, Pan Yutian, Fu Yuyan. "Study on resistance calculation and prediction of amphibious vehicle based on CFD," Journal of Gun Launch & Control, vol. 33, no. 4, pp1-4, 2012

[12] Wang Tao, Guo Qisheng, Xu Guoying. "Simulation of flow field of amphibious vehicle on water," Journal of System Simulation, vol. 19, no. 22, pp5130-5132+5153, 2007

[13] Li Li, Bi Xiaoping, Jia Xiaoping. "Numerical simulation of resistance of tracked amphibious vehicle in sailing," Shipbuilding of China, vol. 44, no. 4, pp47-50, 2003

[14] Xin Z, Su D. "Analysis and research on vehicle wading performance," Proceedings of the Institution of Mechanical Engineers, Part D: Journal of Automobile Engineering, vol. 235, no. 1, pp3-15, 2021

[15] Amini Foroushani J, Sabzpooshani M. "An approach for the estimation of hydrodynamic coefficients of an underwater vehicle in off-design velocities," Journal of Marine Science and Technology, vol. 26, no. 2, pp368-381, 2021

Zhanlong Li, male, became a member of IAENG in 2024. He was born on November 14, 1985, in Shuozhou City, Shanxi Province, China. In 2016, Li received his PhD in Vehicle Engineering from Xi'an University of Technology, Xi'an, Shaanxi Province, China. His main research topics include the design theory and methods of special vehicles and emergency equipment.

Zhanlong Li as currently the director of the Intelligent Transportation Equipment Research Institute at the School of Vehicle and Transportation Engineering, Taiyuan University of Science and Technology. And he is deputy general manager of Shanxi Intelligent Transportation Laboratory Co., Ltd., Taiyuan 030036, P.R. China. And Selected publications:

(1) Zhanlong Li, Shixun Zhao, Bao Sun, et al. “Performance and Optimization of the Hydropneumatic Suspension of High-Speed Wheeled Excavators” Engineering Letters, 2023, vol. 31, no.2, pp674-680, 2023

(2) Zhanlong Li, Zheng Zhang, Zhizhao Ren, et al. “Research on damage behavior of silicone rubber under dynamic impact” International Journal of Non-Linear Mechanics, vol. 164, no.104775 ,2024.

(3) Li Zhanlong, Ren Zhizhao, Zhang Haiqing, Zhang Zheng and Song Yong, “Dynamic Characteristics and Optimization of Segmented Fork Arm Seat System” International Journal of Acoustics and Vibration, vol. 28, no.4, pp381–393, 2023

His research interests include key technologies for high-end emergency rescue equipment, special carrier platforms and their integrated application technologies, vehicle vibration and structural optimization design, and new energy drive technology, among others. Dr. Zhanlong Li is also the Secretary General of the Shanxi Province Society of Automotive Engineers, China.